PHYSICAL REVIEW B **96**, 214102 (2017)

Structural transformations in (1-x)$Na_{0.5}Bi_{0.5}TiO_3$-$x$$BaTiO_3$ single crystals studied by Raman spectroscopy

G. de la Flor,[1,2,*] T. Malcherek,[1] S. Gorfman,[3] and B. Mihailova[1]
[1]*Department of Earth Science, University of Hamburg, Hamburg 20146, Germany*
[2]*Departamento de Física de la Materia Condensada, Universidad del País Vasco UPV/EHU, Bilbao, Spain*
[3]*Department of Materials Science and Engineering, Faculty of Engineering, Tel Aviv University, Tel Aviv 69978, Israel*

(Received 11 September 2017; revised manuscript received 2 November 2017; published 8 December 2017)

Hard-mode Raman spectroscopy was applied to analyze the temperature-induced transformation processes in perovskite-type (ABO_3) single crystals of (1-x)$Na_{0.5}Bi_{0.5}TiO_3$-$x$$BaTiO_3$ (NBT-xBT) in a wide temperature range between 100 and 1010 K and a composition range of $x = 0$–0.074 across the morphotropic phase boundary (MPB). The results show abundant uncoupled ferroic structural distortions even at 1010 K and coexistence of two types of mesoscopic-scale ferroic order at lower temperatures. Octahedral BO_6 tilting is typical of pure NBT, while the incorporation of A-site Ba^{2+} suppresses the tilting and promotes the off centering of BO_6 octahedra. The temperature evolution of the phonon modes clearly reveals the two macroscopically observed critical temperatures T_m and T_d as well as, in the case of $x \neq 0$, two characteristic temperatures T' and T'' preceding the T_m and T_d, respectively, which are attributed to mesoscopic-scale antiferroelectric and ferroelectric coupling processes within the A-site-cation subsystem. At $x < x_{\mathrm{MPB}}$ the two sublattices, off-centered A-site cations and off-centered B-site cations, remain incoherent in the entire temperature range. Only when the amount of Ba reaches x_{MPB} the two subsystems couple dynamically, which can explain the enhancement of properties at the MPB. The overall ferroic distortion, however, has a minimum at the MPB, probably because at x_{MPB} the ferroelectric coupling between B-site Ti^{4+} cations is reduced to a greater extent than the enhancement of ferroelectric coupling between A-site Bi^{3+} cations.

DOI: 10.1103/PhysRevB.96.214102

I. INTRODUCTION

The ferroelectric solid solution (1-x)$Na_{0.5}Bi_{0.5}TiO_3$-$x$$BaTiO_3$ (NBT-xBT), which exhibits a morphotropic phase boundary (MPB) and a rich composition-temperature (x-T) phase diagram [1–3], is considered as a promising environmentally friendly replacement for Pb-based ferroelectric materials. Even though NBT-xBT has been extensively investigated, there is still controversy in the literature concerning the basic structural features, such as the sequence of temperature-induced phase transitions, the type of ferroic long-range order, the stability of the phases, and their relation to the macroscopic properties [4–7]. There is no consensus even whether the frequency dispersion of the dielectric permittivity is related to a weak relaxor state [8,9] or arises from domain-wall relaxation [10]. To a certain extent, the divergence of opinions is related to three factors: (i) the sample type – ceramics or single crystals [11], (ii) the preparation method [12], and (iii) the analytical methods used to characterize the structure, since different techniques may give different pictures of the same system depending on the length and time scale of sensitivity of the method [13]. It should be emphasized that NBT-xBT single crystals exhibit stronger higher piezoelectric effect than ceramics [14]. Furthermore, the reported MPB composition x_{MPB} for single crystals is $x_{\mathrm{MPB}} \sim 0.050$–0.055 [11,14], i.e., slightly below the common value for ceramics $x_{\mathrm{MPB}} \sim 0.060$ [1].

High-resolution single crystals and powder-diffraction studies [15–18] along with optical linear birefringence [19] have shown that the room-temperature average structure of pure NBT is monoclinic Cc (no. 9), having a $a^-a^-c^-$ BO_6 tilt pattern. At room temperature this monoclinic structure undergoes a series of composition-induced phase transitions, related to the change in the BO_6 tilt order, when BT is added: at $x \sim 0.03$–0.04 the BO_6 tilt pattern transforms to $a^-a^-a^-$, which gives rise to rhombohedral $R3c$ symmetry of the average structure; then at $x \sim 0.05$–0.06 $a^0a^0c^+$ tilt order occurs, changing the symmetry to tetragonal $P4bm$; and finally at $x \sim 0.10$–0.11 the BO_6 tilting vanishes and a polar structure of tetragonal $P4mm$ symmetry is stabilized [20]. Recent studies combining nuclear magnetic resonance spectroscopy and *ab initio* calculations, however, showed that tilt disorder rather than a definitive long-range tilt order should exist near the MPB [9].

Two critical temperatures can be deduced from the comprehensive analyses of dielectric properties: depoling temperature T_d, at which the dielectric permittivity exhibits a small hump and above which the spontaneous net polarization is suppressed, and the temperature of the dielectric permittivity maximum T_m [3,8,11,21–25]. The depoling temperature T_d defines the ferroelectric-antiferroelectric (FE-AFE) phase transition, whereas T_m corresponds to the antiferroelectric-paraelectric (AFE-PE) transition. However, structural investigations have not revealed any change in the long-range order precisely at T_d [3]. Ma *et al.* [26] have proposed the term *relaxor antiferroelectric* to describe the behavior of the NBT-xBT system between T_d and T_m. While relaxor ferroelectrics are typically considered to contain FE nanodomains/polar nanoregions dispersed in a cubic matrix [27,28], in relaxor

---

[*] gemma.delaflor@uni-hamburg.de

antiferroelectrics the displacements of the A-site cations (Bi^{3+}, Na^{+}, Ba^{2+}) are antiparallel to the displacements of the B-site cations (Ti^{4+}) within each individual nanodomain, resulting in AFE-type nanodomains. It is worth noting that recently it was proposed that the polar nanoregions in Pb-based relaxor ferroelectrics are in fact *ferrielectric* in nature [29,30], which combines the underlying ideas of both concepts.

The fact that the existence of the AFE state cannot be clearly detected by conventional diffraction methods highlights the importance of ferroic coupling on the mesoscopic scale and calls for the application of methods sensitive to the local structure and dynamics. Raman spectroscopy has been proven to be a powerful method for analyzing the mesoscopic-scale structure and transformation processes via following the temperature or pressure dependencies of phonon anomalies and their renormalization under an external electric field or composition [31–35]. There are plenty of Raman and infrared studies of pure NBT but to the best of our knowledge Raman spectroscopy has never been used to study NBT-xBT single crystals as a function of temperature over a composition range across the MPB. Such studies have been reported only for NBT-xB ceramics [36,37], but strictly speaking the vibrational states in ferroelectric ceramics are represented by quasiphonons of mixed symmetry and polarization [38], i.e., spectroscopic analyses of ceramics provide an average picture over intensities and wave numbers of crystal eigenmodes. Therefore polarized Raman spectroscopic studies on single crystals are required to better elucidate the chemical effect on the crystal atomic dynamics as well as on the temperature-driven coupling processes in the crystal bulk and their relation to the enhanced physical properties near the MPB.

This paper reports on the temperature-driven structural transformations in NBT-xBT single crystals studied by *in situ* polarized Raman spectroscopy over a temperature range from 100 to 1010 K and a composition $x \in (0,0.075)$. We found that the temperature evolution of specific phonon modes clearly reveals both critical temperatures, including T_d that cannot be detected via conventional Bragg diffraction analysis, as well as the mesoscopic-scale coupling phenomena responsible for the corresponding phase transitions. The comparison between the temperature trends of low-energy phonon modes for different compounds further elucidates the atomistic mechanism of the composition-driven crossover from monoclinic to tetragonal ferroelectric long-range order.

II. EXPERIMENTAL DETAILS

NBT-xBT single crystals were synthesized by the top seeded solution growth method [39]. The chemical composition was verified by electron microprobe analysis (EMPA) using a wavelength-dispersive Cameca Microbeam SX100 scanning electron microscopy system and averaging over ~100 points for each compound.

The average structural metrics of the samples was checked by single-crystal x-ray diffraction (XRD) at room temperature. Monochromatic Mo K_α radiation ($\lambda = 0.7107$ Å) was obtained with a graphite monochromator on a Nonius KappaCCD diffractometer. Full limiting spheres of diffraction data up to a maximum theta angle of 40° were collected with a crystal to detector distance of 50 mm. Reflection positions were analyzed by profile fitting with the EVAL15 suite of programs [40] and indexed using a primitive perovskite unit cell. At the available resolution, the lack of significant splitting of reflections did not permit peak modeling using multiple domains of appropriate symmetry. Lattice parameters were therefore refined without symmetry constraints to capture the average peak positions, using all reflections above the sigma level.

Parallel (HH) and cross (VH) polarized Raman spectra were collected in backscattering geometry with a Horiba Jobin-Yvon T64000 triple-grating spectrometer equipped with an Olympus BH41 microscope and a 50x long-working-distance objective. The Raman scattering was excited with the 514.5-nm line of an Ar^{+} laser (Coherent Innova 90C FreD). The achieved spectral resolution was $\sim 2\ \mathrm{cm}^{-1}$, while the precision in the peak position was $0.35\ \mathrm{cm}^{-1}$. At room temperature all Ba-containing compounds exhibited pseudocubic Raman scattering, i.e., the set of parallel and cross polarized spectra, were the same, independently of the orientation of the third dimension of the crystal specimen with respect to the direction of laser propagation. Furthermore, the room-temperature angular dependence of the depolarization ratio $I_{\mathrm{VH}}/I_{\mathrm{HH}}$ did not provide any indications of ferroic multidomain patterns for all crystals with $x \neq 0$. Thus, the HH and VH spectra can be considered to correspond to $\bar{Z}(XX)Z$ and $\bar{Z}(YX)Z$ (Porto's notations), with X, Y, and Z parallel to the pseudocubic $\langle 100 \rangle$ directions.

In situ temperature-dependent experiments were in a LINKAM THMS-E600 and a LINKAM TS1200 EV-1015 stage in the ranges 100–870 and 800–1010 K, respectively, with a heating/cooling rate of 10 K/min and a temperature accuracy of ±0.1 K. The reversibility of the observed temperature-induced structural changes was verified by measuring the room-temperature spectrum at the end of each run. Raman spectra of all compounds were collected on cooling. Since below room temperature the crystals with $x = 0$ and 0.013 developed a micrometer- or submicrometer-scale domain texture that could be visually observed, these samples were also measured on heating from 100 K up, to ensure collection of Raman scattering from the same single domain. According to acoustic emission studies on NBT-xBT single crystals, the difference between the critical temperatures detected on cooling and heating is ~10 K [41]. Since the temperature step in our experiments was 10 K, the expected uncertainty in the characteristic temperatures is also approximately 10 K, which allows the comparison of the values derived from data sets collected on cooling and heating.

The measured spectra were temperature reduced by the Bose-Einstein occupation factor, using the relation $I_{\mathrm{reduced}} = I_{\mathrm{measured}}/\{[\exp(\hbar\omega/kT) - 1]^{-1} + 1\}$, where $\hbar$, ω, k, and T are the reduced Planck constant, phonon wave number, Boltzmann constant, and temperature, respectively. The spectra were then fitted with pseudo-Voigt functions $\mathrm{PV} = qL + (1 - q)G$ ($q \in [0,1]$, where L and G stand for Lorentzian and Gaussian, respectively) to determine the phonon wave number ω, full widths at half maximum (FWHMs), integrated intensities I, and the Lorentzian weight coefficients q. The criterion for the maximum number of peak functions used to fit each spectrum profile was $dI/I < 1$ for all peaks, where I and dI are the magnitude and absolute error of the peak integrated intensity derived from the fitting [37].

TABLE I. Content of Ba in atoms per formula unit (apfu), which determines the value of x, and Na/Bi ratio calculated from EMPA data.

Compound	Ba content (apfu)	Na/Bi
NBT	0	0.98 ± 0.03
NBT-0.013BT	0.013 ± 0.002	0.97 ± 0.03
NBT-0.048BT	0.048 ± 0.002	1.02 ± 0.03
NBT-0.053BT	0.053 ± 0.002	1.01 ± 0.02
NBT-0.074BT	0.074 ± 0.007	1.00 ± 0.10

III. RESULTS AND DISCUSSION

The performed EMPA has confirmed that the NBT-xBT single-crystal samples are chemically homogeneous and the ratio between Na and Bi is unity within uncertainties (see Table I). The exact value of x for each sample was determined from the amount of Ba in atomic units (Table I).

According to in house single-crystal XRD, all samples exhibit pseudocubic structure at room temperature. It should be emphasized that it was not possible to refine the actual crystal structure due to the multidomain texture and thus the lattice parameters given here only represent the average over domains. Nevertheless the composition trends are reliable, since the analyses of all compounds have been done in the same manner, without any symmetry constraints. As can be seen in Fig. 1(a), the three unit-cell vectors have the same magnitude $a = b = c$ for all studied compounds, but the nonlinear trend with x indicates subtle composition-induced changes in the unit-cell metrics. Furthermore, the derived effective unit-cell angles deviate from 90° for $x = 0$, 0.013, and 0.048, while for $x = 0.053$ and 0.074 the unit-cell angles are equal to 90° [Fig. 1(b)] within the uncertainties. The latter matches tetragonal symmetry among the possible polar crystal classes of the perovskite structure type. Zhang *et al.* have previously reported that the MPB for single crystals is slightly lower than that for ceramics and it should be closer to $x = 0.05$ rather than to 0.063 typical of ceramics [11]. Our data also suggest that the structure has a nonorthogonal metrics for $x < 0.05$ and an orthogonal one for $x > 0.05$, which asserts that the MPB for single crystals is in the vicinity of $x = 0.05$. Another interesting observation is that the average deviation of the unit-cell angles from 90° initially increases upon Ba doping, but the trend reverses between $x = 0.013$ and 0.048 [Fig. 1(b)]. Similar enhancement of the nonorthogonality at $x \sim 0.03$ has been deduced from structure refinements to synchrotron XRD data [42]. The composition dependence of the unit-cell size also exhibits an anomaly at $x \sim 0.03$ [Fig. 1(a)]. A change in the BO_6 tilt pattern near $x = 0.03$–0.04 has been previously proposed on the basis of transmission electron microscopy analyses [20] and such a modification in the long-range order might be the reason for the observed composition dependence of the room-temperature lattice parameters for x between zero and 0.05.

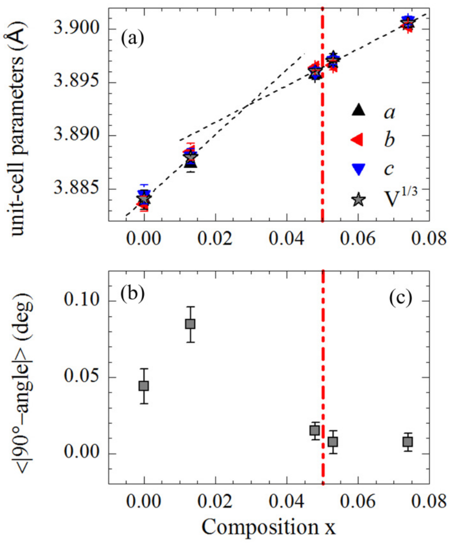

FIG. 1. Composition trends of the room-temperature effective unit-cell parameters a, b, c along with the cube root of the unit-cell volume (a) and the average angle deviation from 90° (b) of NBT-xBT derived from unconstrained unit-cell refinements to single-crystal XRD data. The vertical dash-dotted lines mark the MPB composition in single crystals after Zhang *et al.* [11].

Figure 2 compares the room-temperature Raman spectra of NBT-0.05BT ceramic and NBT-0.048 single crystal. As can be seen, the Raman scattering collected from a polycrystalline sample is a superposition of the parallel and cross polarized spectra collected from a single crystal. The major difference between the ceramic and single-crystal spectra is in the peak intensity ratio in the range 550–650, 240–310, and 30–60 cm^{-1}, arising from internal BO_6 modes, phonon modes comprising mainly B-site cation vibrations, and phonon modes comprising mainly A-site cation vibrations, respectively (see Table II). The variation in the intensity ratios is related to the symmetry of phonon modes and the actual magnitudes of the corresponding polarizability-tensor components allowed to be observed in specific scattering geometry [43]. Moreover, in ceramics composed of ferroelectric crystalline grains quasiphonons of mixed symmetry and mixed polarization averaged over all random orientations are measured. In contrast, pure phonons can be measured from properly oriented single-domain single-crystal specimens or, in the case of multidomain single crystals, quasiphonons averaged only over the symmetry allowed directions are measured. Since the wave numbers of quasiphonons depend on the orientation of the wave vector to the unit-cell polarization [38], the peak positions measured from ferroelectric ceramics may differ from those measured on ferroelectric single crystals. Hence, even the peak positions measured from ferroelectric ceramics can be different from those collected from single crystals at the same temperature, which may also lead to difference in the spectrum profile and even in the overall shape of the temperature trends.

The temperature-reduced polarized Raman spectra of NBT-xBT measured at different temperatures are shown in Fig. 3. Above 750 K the average structure of all five compounds is cubic with space group $Pm\bar{3}m$ and therefore no Raman-active modes are allowed in either scattering geometry. However, all compounds exhibit pronounced Raman scattering in both parallel (HH) and cross polarized (VH) configurations even at 1010 K (Fig. 3). Moreover, the total Raman intensity calculated as the sum of the integrated intensities in parallel and cross polarized spectra is almost constant in the entire

TABLE II. Peak positions (cm^{-1}) in parallel (HH) and cross polarized (VH) Raman spectra measured at room temperature for NBT-xBT single crystals.

Peak	$x = 0$		$x = 0.013$		$x = 0.048$		$x = 0.053$		$x = 0.074$		Type of vibration
	HH	VH	HH	VH	HH	VH	HH	VH	HH	VH	
1	34.4	32.9	30.4	31.8							Off-centered A-site cations
2	59.7	55.4	57.3	54.2	51.9	41.7	51.3	42.2	52.1	41.5	
3	138.4	138.4	137.2	136.1	119.9	115.9	116.12	114.9	114.1	112.4	A-BO$_3$ translations
3a						162.8		160.5		162.5	
4		251.4			245.1	248.8	250.5	248.5	252.7	251.3	Off-centered B-site cations
5	290.5	298.6	291.4	283.3	311.5	306.6	314.6	308.1	316.6	312.3	
6	400.2		406.5								BO$_6$ tilting
7		473.8	490.0		495.2	468.6	500.8	471.0	499.9	469.2	Internal BO$_6$ vibrations
8	506.5	521.9	524.4	529.6	578.4	531.5	586.0	529.8	582.0	534.8	
9	589.6	570.9	586.6	604.3	620.4	601.3	620.8	594.1	623.2	612.5	
10	770.7	771.3	776.4	768.2	774.0	749.9	776.8	756.6	773.2	749.2	
11	856.7	850.3	858.6	858.0	860.8	846.3	859.9	843.9	859.8	844.0	
12	1038.7		1027.8	1029.0	1023.2		1018.3		1018.4		Second-order Raman

temperature range 100–1010 K and considerably differs from zero (Fig. 4). Since no Raman peaks should be observed for ABO$_3$ materials with $Pm\bar{3}m$ symmetry, the total Raman intensity can serve as a measure of the overall ferroic structural distortion. Therefore, for all compounds in the range $x = 0$–0.074 the high-temperature local structure strongly deviates from the average cubic structure. Furthermore, almost the same total intensity was collected at ~1000 K (macroscopically paraelectric state) and at ~100 K (well-developed ferroelectric state), which clearly points out that the high-temperature structure of NBT-xBT is abundant with uncoupled local ferroic distortions. This already indicates that the temperature-driven phase transitions are of order-disorder rather than displacive character [31,32]. The inset in Fig. 4 shows the evolution of the total intensity with composition. The total intensity exhibits a clear minimum at MPB, which means that the extent of ferroic structural distortion significantly decreases at the MPB.

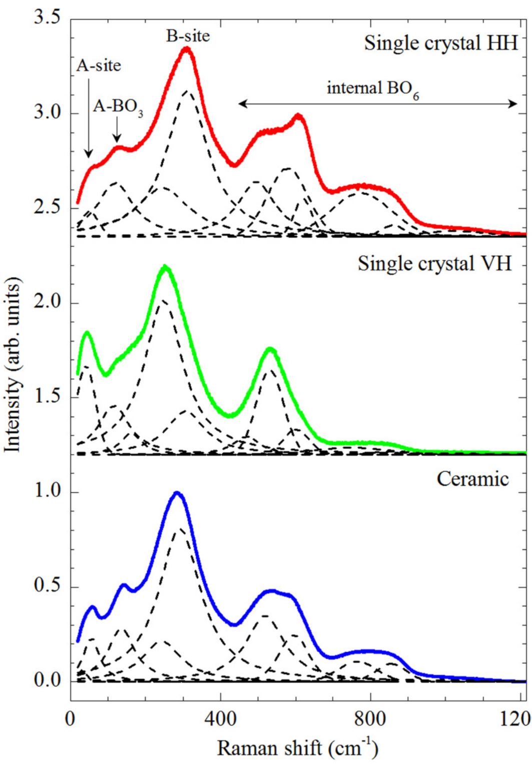

FIG. 2. Room-temperature Raman spectra of a NBT-xBT single crystal with $x = 0.048$ and ceramic with $x = 0.05$; dashed lines represent the fitting pseudo-Voigt functions. The spectra were normalized to unity and vertically offset for clarity. The room-temperature peak positions for all single crystals studied here are given in Table II.

The depolarization ratio $I_{\mathrm{VH}}/I_{\mathrm{HH}}$ is also shown in Fig. 4. In general, this quantity provides information on the development of ferroic long-range ordered domains [29]. An increase in the depolarization ratio measured in the scattering geometry used here indicates occurrence of nontetragonal ferroic domains in the perovskite structure, because such domains are inclined with respect to the pseudocubic $\langle 100 \rangle$ directions and can contribute to both $\bar{Z}(XX)Z$ and $\bar{Z}(YX)Z$ spectra. Indeed, at low temperatures $I_{\mathrm{VH}}/I_{\mathrm{HH}}$ increases for $x = 0$ and 0.013, as the change is much stronger for $x = 0.013$. The larger $I_{\mathrm{VH}}/I_{\mathrm{HH}}$ for $x = 0.013$ at low temperatures can result from greater abundance of ferroic domains and/or larger ferroic distortion of the individual domains. We suggest that the latter is the primary reason for the enhanced depolarization ratio for $x = 0.013$, because the unit-cell angle difference derived from XRD analyses (Fig. 1) indicates a larger nonorthogonal unit-cell distortion at this composition.

Both the parallel (HH) and cross polarized (VH) spectra were analyzed for all compounds. However, for conciseness, in the discussion below we will consider only the data derived from parallel polarized Raman scattering, because the cross polarized spectra do not provide any further essential information.

The overall ferroic distortion of the perovskite structure can be considered in terms of three major types of local distortions: (i) off-center displacements of the A-site cations, (ii) off-center shifts of the B-site cations, and (iii) BO$_6$ octahedral tilts. Thus, in order to follow the composition dependence of the

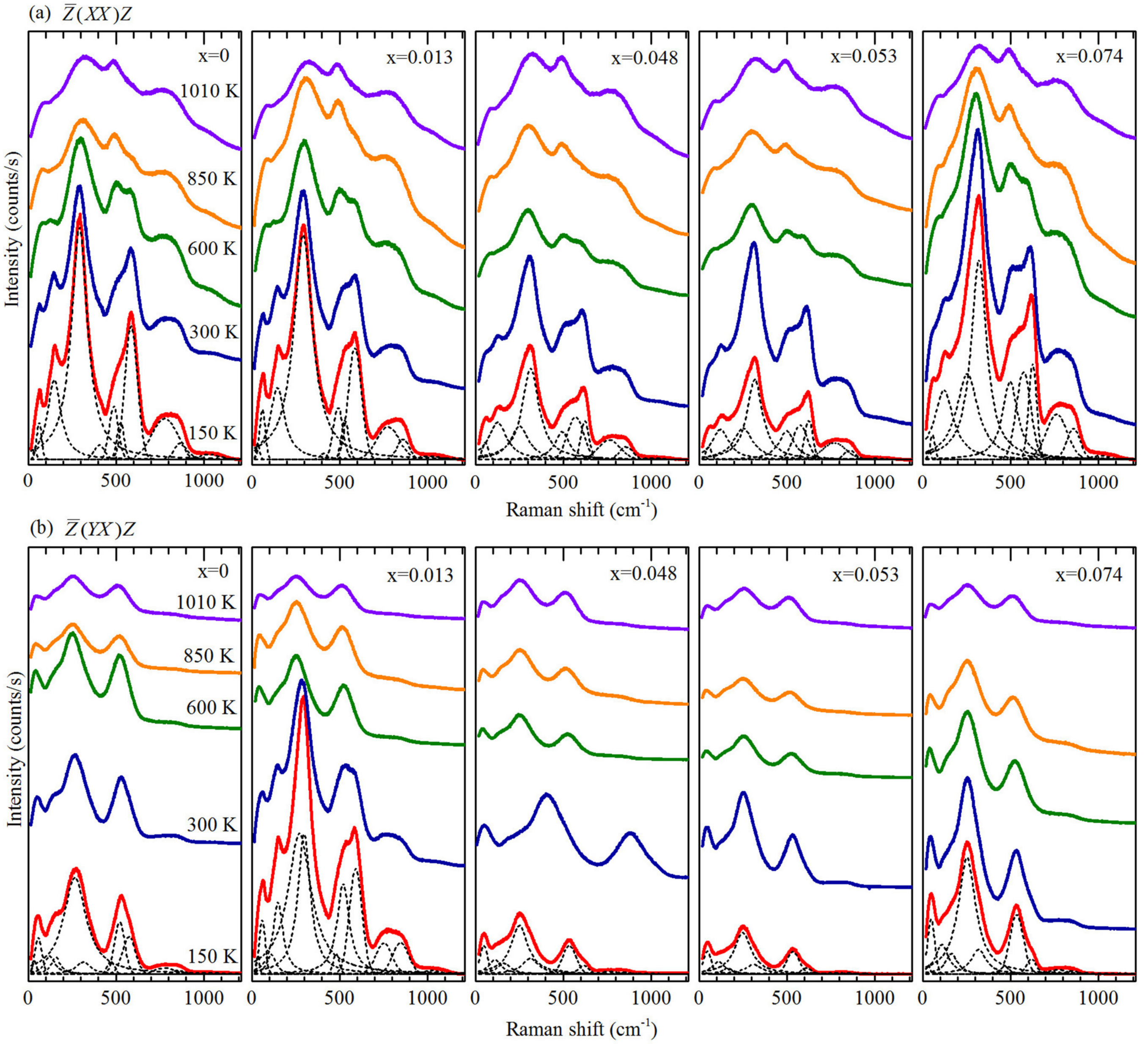

FIG. 3. Representative parallel $\bar{Z}(XX)Z$ (a) and cross polarized $\bar{Z}(YX)Z$ (b) Raman spectra measured at different temperatures between 100 and 1010 K for NBT-xBT with $x = 0$, 0.013, 0.048, 0.053, and 0.074; dashed lines represent the fitting pseudo-Voigt functions at 150 K. The spectra are vertically offset for clarity.

temperature-driven coupling processes, we have focused on the modes associated to those distortions [37,44–46] (see Fig. 5): (1) the phonon modes in the range 30–60 cm^{-1}, which involve mainly the A-site cations and are hence sensitive to A-cation off centering; (2) the phonon modes in the range 240–310 cm^{-1}, which comprise mainly vibrations of B-site cations and are therefore sensitive to B-cation off centering; (3) the A-BO$_3$ translation mode ~150 cm^{-1}, which consists of out-of-phase TiO$_3$ and Bi^{3+}-cation vibrations, i.e., it involves vibrations of both A- and B-site cations and is thus sensitive to coupling processes between off-centered A-site and B-site cations; and (4) the BO$_6$ tilting mode resulting in Raman scattering ~400 cm^{-1}, which can also be considered as A-O bond stretching—Raman scattering from this mode was detected only for NBT $-$ xBT single crystals with $x = 0$ in the entire temperature range as well as for $x = 0.013$ at $T < T_d$; this mode could not be discriminated in the Raman spectra of NBT $-$ xBT powders [37] due to peak overlap. In NBT $-$ xBT the vibrations associated with the A-site and B-site cations are dominated by the ferroelectrically active Bi^{3+} and Ti^{4+}, respectively [37].

Figure 6 shows the temperature dependence of the wave number ω, FWHM Γ, and fractional intensity I_n of Raman scattering near 50 cm^{-1} assigned to the Bi-localized mode. For all compounds this mode softens with the temperature decrease until it reaches a minimum in $\omega(T)$ at a temperature point below T_d and splits into two components at ω_1 and ω_2. For all Ba-containing compounds, $\omega_2(T)$ exhibits linear softening

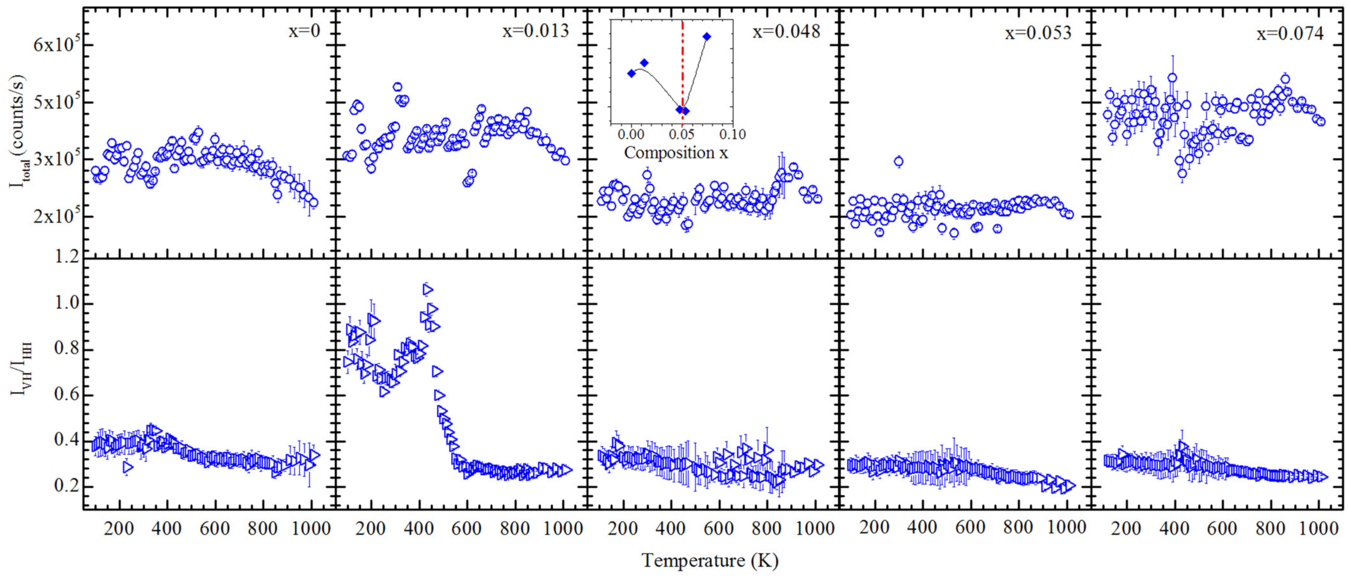

FIG. 4. Total intensity $I_{\mathrm{total}}(T) = I_{\mathrm{HH}}(T) + I_{\mathrm{VH}}(T)$ (upper plots) and depolarization ratio $I_{\mathrm{VH}}(T)/I_{\mathrm{HH}}(T)$ (bottom plots) as a function of temperature for NBT $-$ xBT with $x = 0$, 0.013, 0.048, 0.053, and 0.074. The inset shows the variation of the total intensity with composition $I_{\mathrm{total}}(x)$ with intensity values derived from the corresponding linear fits of I_{total}(T) in the range 200–800 K. The dashed line denotes the MPB.

at high temperatures, which is followed by a considerably nonlinear trend on further temperature decrease. This suggests that on cooling down from ~1000 to 300–400 K two successive coupling processes involving A-site Bi^{3+} cations occur in Ba-doped NBT, in contrast to pure NBT for which a gradual linear softening of $\omega_2(T)$ is observed on approaching the minimum wave-number value. The temperature dependence of Γ_2 as well as of I_{n2} confirms that the addition of Ba induces two transformation processes within the A-site sublattice: for $x = 0$ both $\Gamma_2(T)$ and I_{n2} exhibit only one maximum, indicating one transformation process within the A-site sublattice, while $\Gamma_2(T)$ as well as I_{n2} show two maxima for all compounds with $x \neq 0$. The excess of the FWHMs was analyzed by hard-mode Raman spectroscopy [47] to gain a deeper insight into the transformation processes. For each compound $\Gamma_2(T)$ was fitted with Gaussian functions (green lines in Fig. 6), using as a baseline polynomial functions (blue lines in Fig. 6) to account for the trivial decrease in Raman peak widths on cooling. In general, the position of the maximum of the individual Gaussian functions fitting $\Gamma(T)$ gives the characteristic temperature at which the corresponding structural transformation takes place, whereas the FWHM and integrated area of the fitting Gaussian functions are indicative of the diffuseness and strength of the transformation processes, respectively. The performed hard-mode spectroscopic analysis reveals that the two transformation processes in the A-site sublattice of Ba-doped NBT occur at $T' > T_m$ and $T'' \in (T_d, T_m)$. The characteristic temperature T'' derived from $\Gamma_2(T)$ matches the temperature at which a kink in $\omega_2(T)$ is observed. For pure NBT $T' \equiv T''$ and it is just above T_m.

Figure 7 depicts the composition dependence of the characteristic temperature, diffuseness, and strength of the transformation processes related to the A-site cations. As can be seen, the diffuseness of the structural transformation at T'' gradually decreases with Ba, whereas the diffuseness of the structural transformation at T' has a minimum at the MPB. The MPB is also marked by the enhanced strength of the transformation process that takes place at T''.

Figure 8 shows the temperature dependencies of ω, Γ, and I_n of the phonon mode near 250–300 cm^{-1}, dominated by vibrations of off-centered B-site Ti^{4+}, as well as of the phonon mode near 400 cm^{-1}, which is related to TiO_6 tilts. For single crystals with $x = 0$ the tilting mode persists in the entire temperature range, while the mode related to off-centered Ti vanishes at T ~1000 K. For $x = 0.013$ the tilting mode is resolved only at temperatures below T_d. For the compounds with higher Ba content ($x = 0.048$, 0.053, 0.074) there was no detectable Raman signal associated with the tilting mode, but splitting of the parallel polarized Raman peak arising from the off-centered Ti vibrations was observed. Therefore, the incorporation of Ba at the A site promotes the Ti off centering at the B site and suppresses the octahedral tilting. The latter is consistent with the suggested tilt disorder in the vicinity of MPB [9]. The effect of Ba doping is most probably due to the relatively large ionic radius of Ba^{2+} and the associated local random stress fields, which induce additional octahedral distortions and hinder the development of octahedral tilts [48]. It is worth noting that thorough studies of Pb-based perovskite-type relaxor ferroelectrics at different temperatures and pressures have shown that high pressure favors BO_6 tilting and reduces the off-centered displacements of B-site cations, whereas low temperature has the opposite effect [44,49–52]. The same competition between the TiO_6 tilting and off-centered B-site Ti can be deduced from the temperature evolution of the Raman scattering of pure NBT single crystals (see Fig. 8). The temperature dependencies of the corresponding fractional intensities clearly show that at high temperatures tilting, i.e., antiferrodistortive distortion, prevails over polar shifts of B-site Ti^{4+} cations. At T_m both local structural distortions coexist in equal weight, and below T_d polar Ti^{4+} displacements become dominant while the TiO_6 tilting almost vanishes.

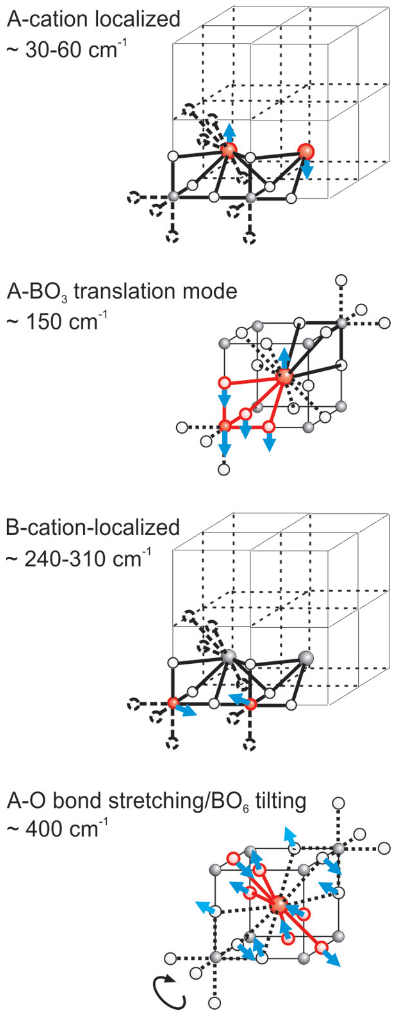

FIG. 5. Sketch of selected phonon modes in complex ABO$_3$-type structures, sensitive to ferroic distortions; mode assignment based on comparison with other perovskite-type ferroelectrics and lattice-dynamics calculations [37,44–46].

It should be noted that for all compounds the two critical temperatures T_d and T_m can be derived from $\omega(T)$ of the B-cation phonon mode (see Fig. 8). For $x = 0$ there is a slight but clear decrease in $\omega_5(T)$ between T_d and T_m, while for $x = 0.013$ $\omega_5(T)$ has a kink at T_m and begins strongly to decrease until reaching a sharp minimum at T_d. For $x = 0.053$ and 0.074, which are above x_{MPB}, the lower-energy component (peak 4) appears exactly at T_m and $\omega_4(T)$ becomes constant at T_d. For $x = 0.048$, which seems to be very close to the MPB composition for single crystals, both $\omega_4(T)$ and $\omega_5(T)$ have a broad minimum with a midpoint at T_d and an extrapolation of $\omega_4(T)$ data to higher temperatures suggests that ω_4 would be equal to ω_5 precisely at T_m.

Independently of the Ba content, there is an excess in $\Gamma_5(T)$ in a wide temperature range. However, in contrast to the A-cation phonon mode near 60 cm^{-1}, $\Gamma_5(T)$ exhibits a single maximum near T' for all five compounds (see Fig. 8). The composition dependence of the characteristic temperature, diffuseness, and strength of this transformation process, as deduced from the position, width and area of the Gaussian fit to $\Gamma_5(T)$, is shown in Fig. 9. For comparison, the characteristic temperature T' related to coupling between the A-site cations is also included in Fig. 9(a). As can be seen, the temperature of the transformation processes at T' differs only for $x = 0.074$, i.e., away from the MPB on the tetragonal side of the x-T diagram. However, unlike the A site (see Fig. 7), the diffuseness of the transformation at the B site increases at the MPB, while the strength of the process decreases. Moreover, the decrease in the strength of the B site at the MPB is much more pronounced than the increase in the A site, which can be the reason for the overall suppression of the ferroic distortion at the MPB (see the inset in Fig. 4) and consequently a structural feature elucidating why the properties of NBT $-$ xBT at the MPB are not as good as those of Pb-based ferroelectric solid solutions.

The analysis of the A- and B-cation phonon modes reveals two mesoscopic-scale processes to occur at $T' > T_m$ and at T'' between T_d and T_m. Characteristic intermediate temperatures have been already reported for pure NBT [53,54] and NBT-0.06BT ceramics [55], but the underlaying mechanism of the structural transformations is still not clarified. For NBT $-$ xBT with a composition close to MPB two characteristic temperatures near 500 and 725 K have been deduced from the temperature dependence of the dielectric permittivity [55], which match well the corresponding values of T'' and T' reported here. The anomalies in the dielectric properties have been attributed to the so-called intermediate temperature $T^{\star}$ and the Burns temperature T_{B}, typical of relaxor ferroelectrics [55]; T_{B} is the temperature at which small dynamic polar clusters nucleate, while $T^{\star}$ is the temperature at which the already existing polar clusters merge into larger polar nanoregions of slower dynamics [49,50,56]. Comprehensive studies of Pb-based relaxors revealed that near $T^{\star} > T_m$ A-site cations with lone-pair electrons preferentially couple antiferroelectrically at an intermediate-range length scale, while B-site cations couple ferroelectrically [30]. However, the temperature-induced pathway of phase transitions of Pb-based relaxor ferroelectrics differs from that in the NBT $-$ xBT system particularly in the absence of a macroscopically detectable AFE state below T_m. Moreover, both $T^{\star}$ and T_{B} are above T_m in the case of Pb-based relaxors, whereas $T'' < T_m < T'$ for NBT $-$ xBT. This implies that straightforward one-to-one analogy between $T^{\star}$ and T_{B} and T'' and T' can hardly be performed and therefore we propose to describe the two transformation processes in NBT $-$ xBT in terms of mesoscopic-scale couplings between different types of off-centered cations. In NBT $-$ xBT solid solution the characteristic temperature T' precedes the PE-to-AFE phase transition at T_m, whereas T'' precedes the AFE-to-FE phase transition at T_d. Therefore, we suggest that T' and T'' in NBT $-$ xBT correspond to a mesoscopic-scale AFE and FE coupling within the sublattice of A-site Bi^{3+} cations, respectively. The off-centred B-site Ti^{4+} cations are involved only in a single transformation process at T', where they couple between each other ferroelectrically. The AFE coupling between A-site cations prevails at T', driving the system on subsequent cooling to a macroscopically nonpolar ferroic state, whereas at T'' the FE coupling between A-site cations becomes dominant, governing the system to a long-range FE order at T_d.

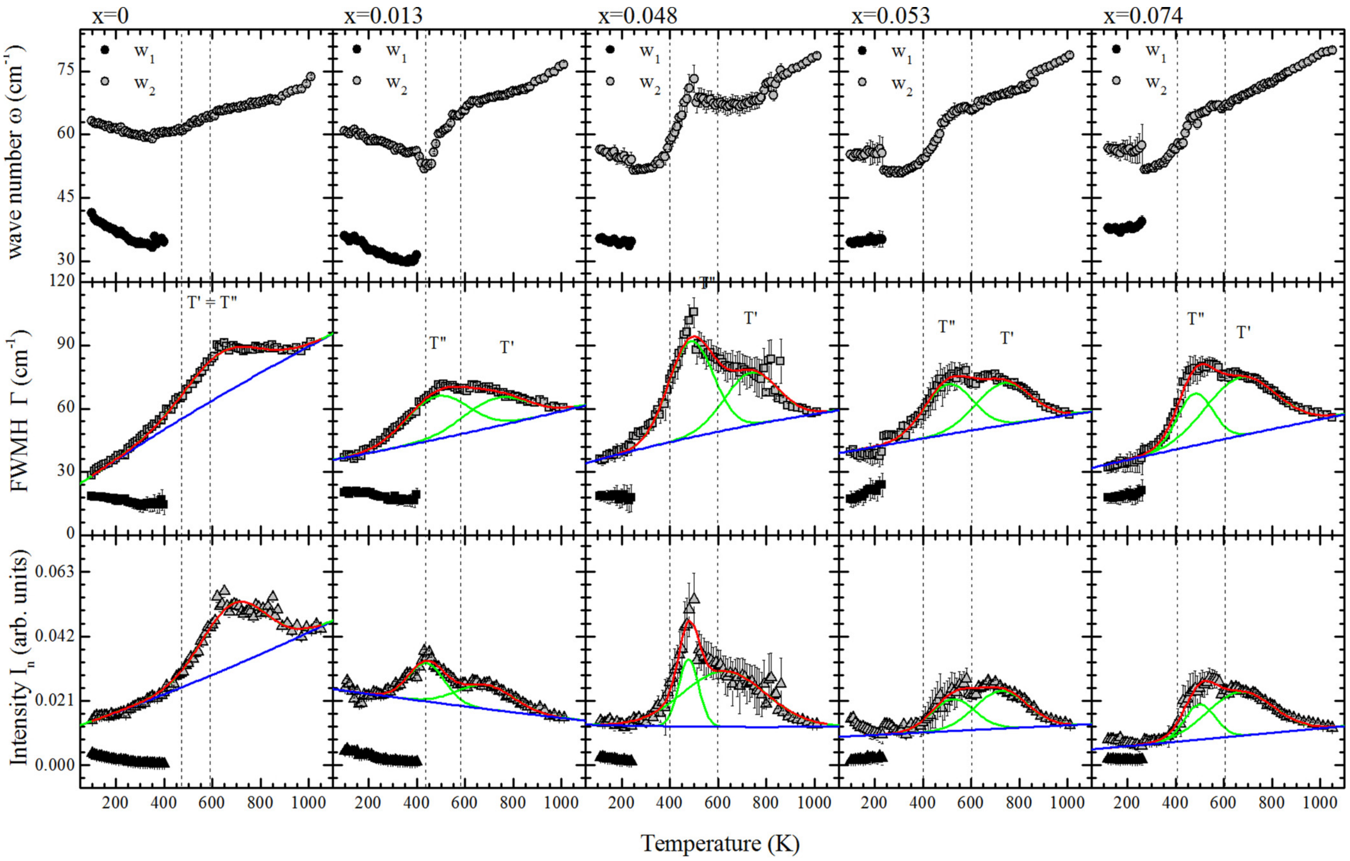

FIG. 6. Temperature evolution of the wave number ω, FWHM Γ, and fractional intensity I_n of the Bi-localized mode in NBT-xBT derived from HH spectra; gray and black symbols represent the higher-energy and lower-energy component, respectively. The green lines correspond to the Gaussian functions fitting $\Gamma(T)$ and $I_n(T)$, after polynomial baseline correction (blue line) to account for the trivial decrease in phonon widths on cooling. The red lines represent the resultant profiles. The vertical dashed lines mark the macroscopic characteristic temperatures T_d and T_m determined by dielectric measurements [2,11,24].

Pure NBT exhibits only one characteristic temperature related to coupling within the A-site cationic system, most probably because of the pronounced octahedral tilting, as indicted by the persistence of the BO_6 tilting mode in the entire temperature range 100–1010 K. The tilt order is antiferrodistortive in nature and hence ensures the coexistence of competing types of ferroic coupling and subsequent development of the AFE state between T_m and T_d. However,

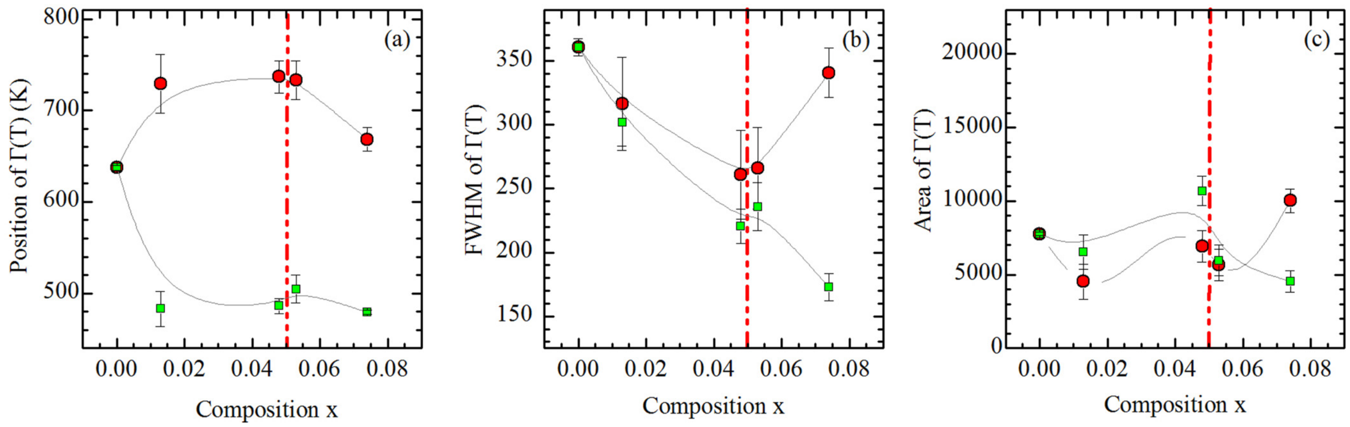

FIG. 7. Composition dependence of the position (a), FWHM (b), and area (c) of the Gaussian functions used to fit the temperature dependence $\Gamma(T)$ of the phonon mode near 60 cm^{-1} involving mainly Bi^{3+}-cation vibrations (see Fig. 6). These parameters represent the characteristic temperature, diffuseness, and strength, respectively, of the structural transformations driven by Bi^{3+} cations. Red circles and green squares correspond to the transformation process that takes place at T' and T'', respectively. The vertical dash-dotted red lines mark the MBP. The black thin lines are B-spline interpolations to guide the eye.

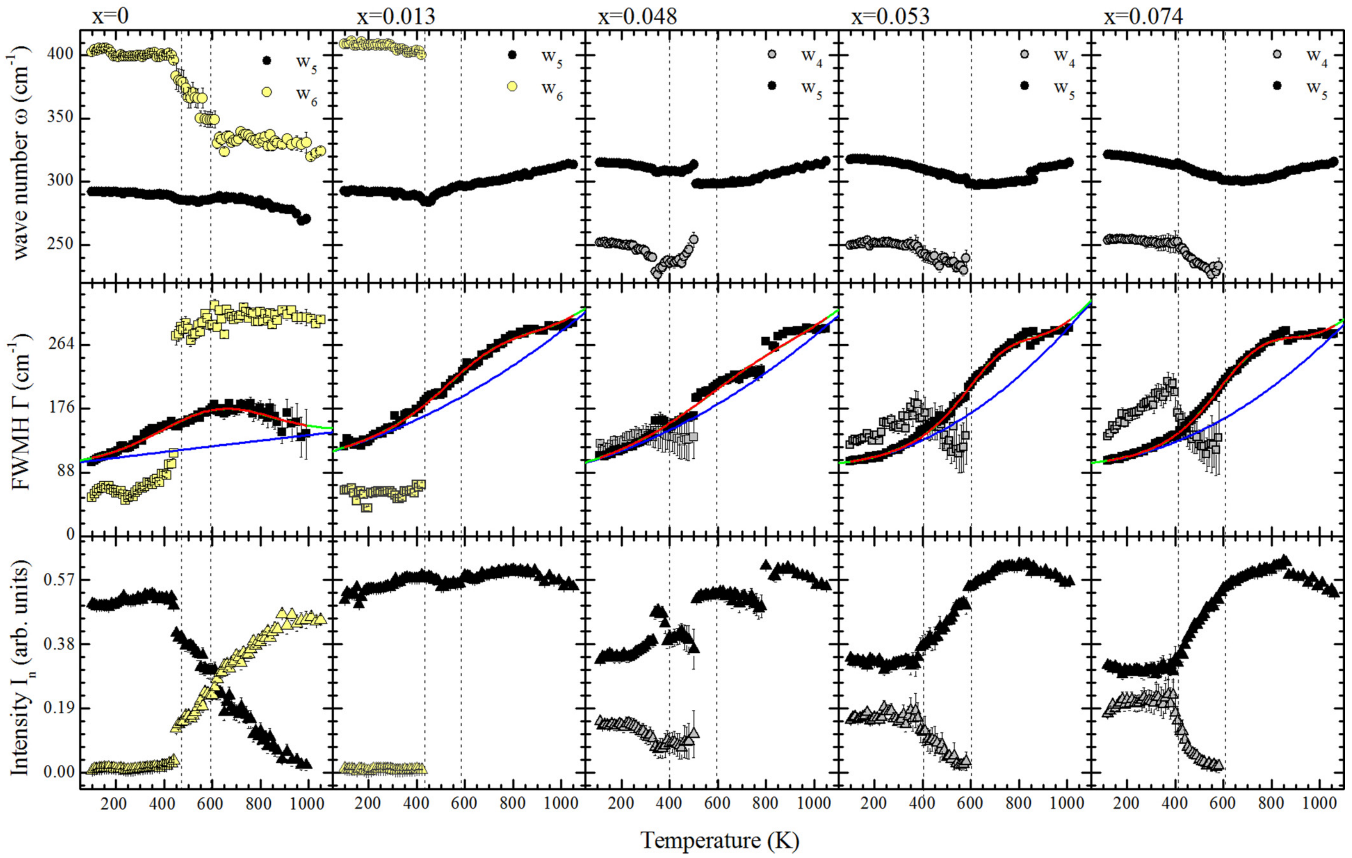

FIG. 8. Temperature evolution of the wave number ω, FWHM Γ, and fractional intensity I_n of the Ti-localized mode and the TiO_6 tilting mode in NBT $-$ xBT derived from HH spectra; yellow symbols represent the tilting mode, and gray and black symbols represent the higher-energy and lower-energy component of the Ti-localized mode, respectively. The green lines correspond to the Gaussian functions fitting $\Gamma(T)$ and $I_n(T)$, after polynomial baseline correction (blue line) to account for the trivial decrease in phonon widths on cooling. The red lines represent the resultant profiles. The vertical dashed lines correspond to the macroscopic characteristic temperatures T_d and T_m determined by dielectric measurements [2,11,24].

further *in situ* Raman studies under an external electric field are necessary to clarify this point.

Now let us consider the temperature dependence of ω, Γ, and I_n of the Bi $-$ TiO_3 translation mode near $150\,\mathrm{cm}^{-1}$ (Fig. 10), involving vibrations of both A-site Bi^{3+} and B-site Ti^{4+}. For $x = 0$ $\omega_3(T)$ exhibits a plateaulike minimum between T_d and T_m, indicating ongoing structural transformations in this temperature range. For $x = 0.013$ $\omega_3(T)$ has

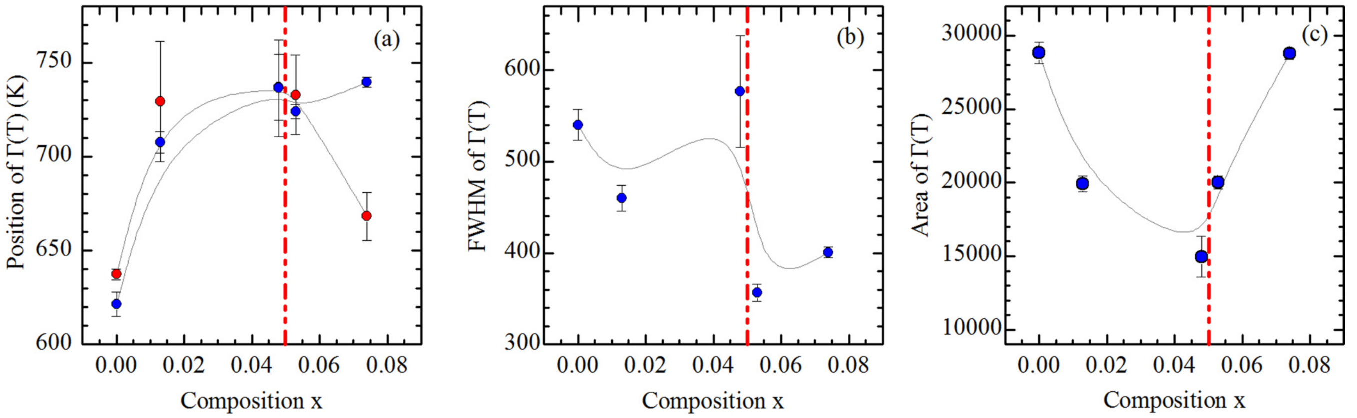

FIG. 9. Composition dependence of the position (a), FWHM (b), and area (c) of the Gaussian function used to fit the temperature dependence $\Gamma(T)$ of the phonon mode near 300 cm^{-1} involving mainly Ti^{4+}-cation vibrations (see Fig. 8). These parameters represent the characteristic temperature, diffuseness, and strength, respectively, of the structural transformations driven by B-site Ti^{4+} cations. For comparison, the characteristic temperatures related to the structural transformation in the A-site cations are also in included in (a) as red circles. The vertical dash-dotted red lines mark the MBP. The black thin lines are B-spline interpolations to guide the eye.

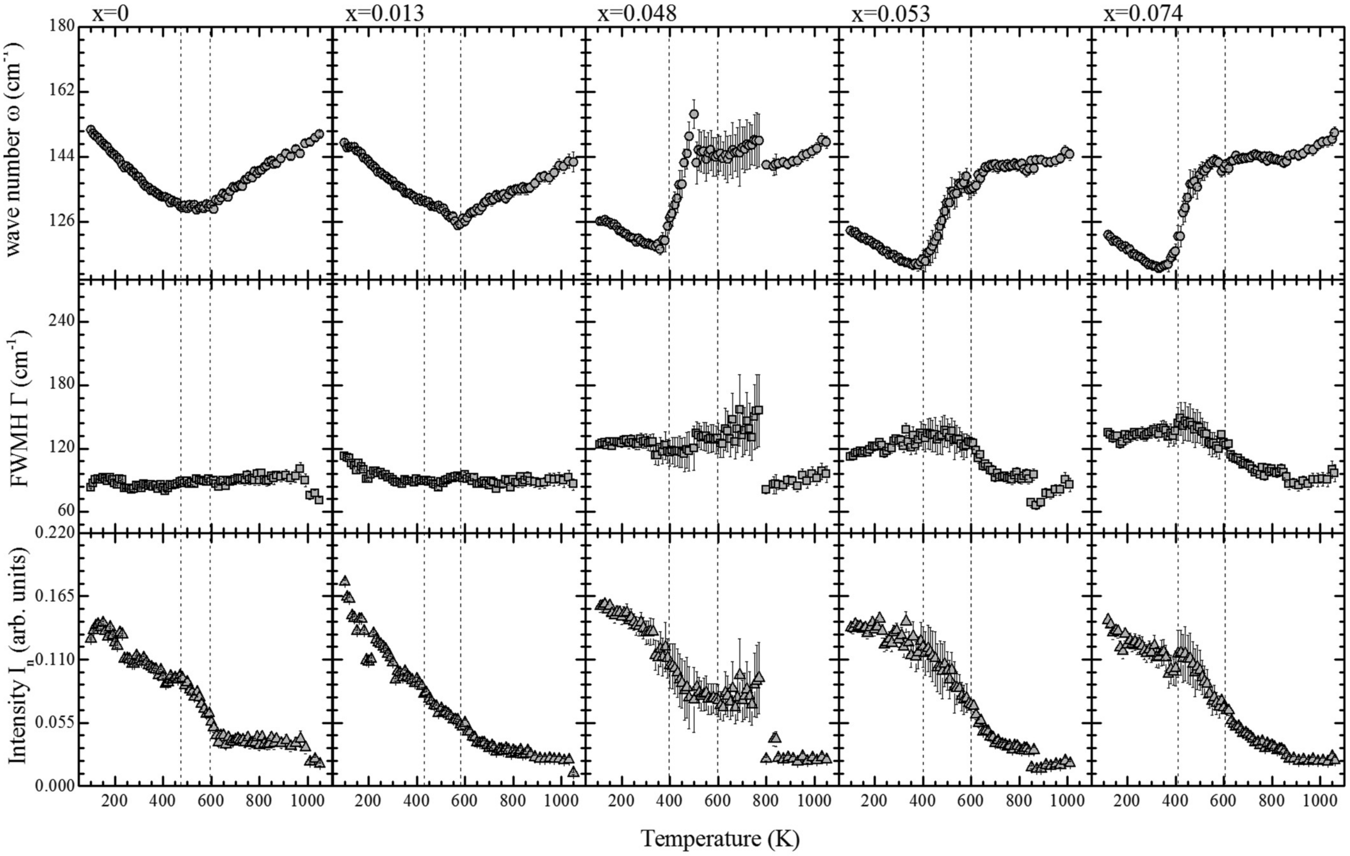

FIG. 10. Temperature evolution of the wave number ω, FWHM Γ, and fractional intensity I_n of the Bi-TiO_3 mode comprising vibrations of both Bi^{3+} and Ti^{4+} cations in NBT $- xB$T derived from HH spectra. The vertical dashed lines mark the macroscopic characteristic temperatures T_d and T_m determined by dielectric measurements [2,11,24].

a minimum near T_m, while for $x = 0.048$, 0.053, and 0.074 $\omega_3(T)$ exhibits more complex behavior, with a kink near T'' and an absolute minimum close to T_d. A well-pronounced minimum in $\omega_{\mathrm{Bi-TiO_3}}$ at T_d has already been reported for NBT $- x$BT ceramics with $x \sim x_{\mathrm{MPB}}$ [37]. The most striking effect related to Ba doping is, however, the change in the trend of $\Gamma_5(T)$: it shows no maximum in the entire temperature range for $x = 0$ and 0.013, indicating that the subsystem of off-centered B-site cations remains incoherent with the subsystem of off-centered A-site cations; the same phenomenon was also observed in ceramics with $x \sim x_{\mathrm{MPB}}$ [37]. Only when approaching the MPB at $x = 0.048$ $\Gamma_5(T)$ exhibits an abrupt increase near T' with temperature, indicating strong coupling between the two subsystems and synchronization of the temperature-induced transformation processes within the A-site and B-site subsystems already above T_m. Further doping with Ba smears out the coupling between off-centered A-site Bi and off-centered B-site Ti in a wider temperature range and shifts the maximum of this process towards T''.

To further elucidate the structural state of NBT $- x$BT and related coupling processes between the two types of ferroelectrically active cations, A-site Bi^{3+} and B-site Ti^{4+}, we have considered the variations of ω and Γ of the Bi-TiO_3 mode with x at fixed temperatures in different temperature ranges: below T_d, between T_d and T'', between T'' and T_m, between T_m and T', and above T' (Fig. 11). Even a small addition of A-site Ba modifies the structural state at high temperatures above T', as revealed by the softening of $\omega_3(x)$ at $x = 0.013$ accompanied by a slight increase in Γ_3. The fractional Raman intensities reveal that TiO_6 tilting is the most pronounced ferroic structural distortion in the high-temperature structural state of pure NBT. Therefore, the softening of the tilting Bi-TiO_3 mode at $x = 0.013$ at high temperatures mirrors the Ba-induced disturbance of the octahedral tilting. The Bi-TiO_3 mode exhibits similar behavior with composition x in the entire temperate range between T' and T'': the Ba-induced softening at low x values is preserved, but there is also slight softening near the MPB accompanied by considerable phonon damping (increase in Γ), indicating significant structural transformations at x_{MPB}. This confirms the suggestion that the coexistence of competing types of local ferroic order in the temperature range (T'', T') hinders the coupling between A-site and B-site cations for $x < x_{\mathrm{MPB}}$ and synchronization between the ferroic orders on the two sublattices is achieved only when Ba content reaches x_{MPB}. In the temperature range (T_d, T'') $\omega_3(x)$ exhibits only one sharp minimum at x_{MPB}, indicating coherence between the FE order in the A-site sublattice and FE order of the B-site sublattice at the MPB. At temperatures below T_d the Bi-TiO_3-phonon softening and damping become more gradual. These composition trends at different temperatures

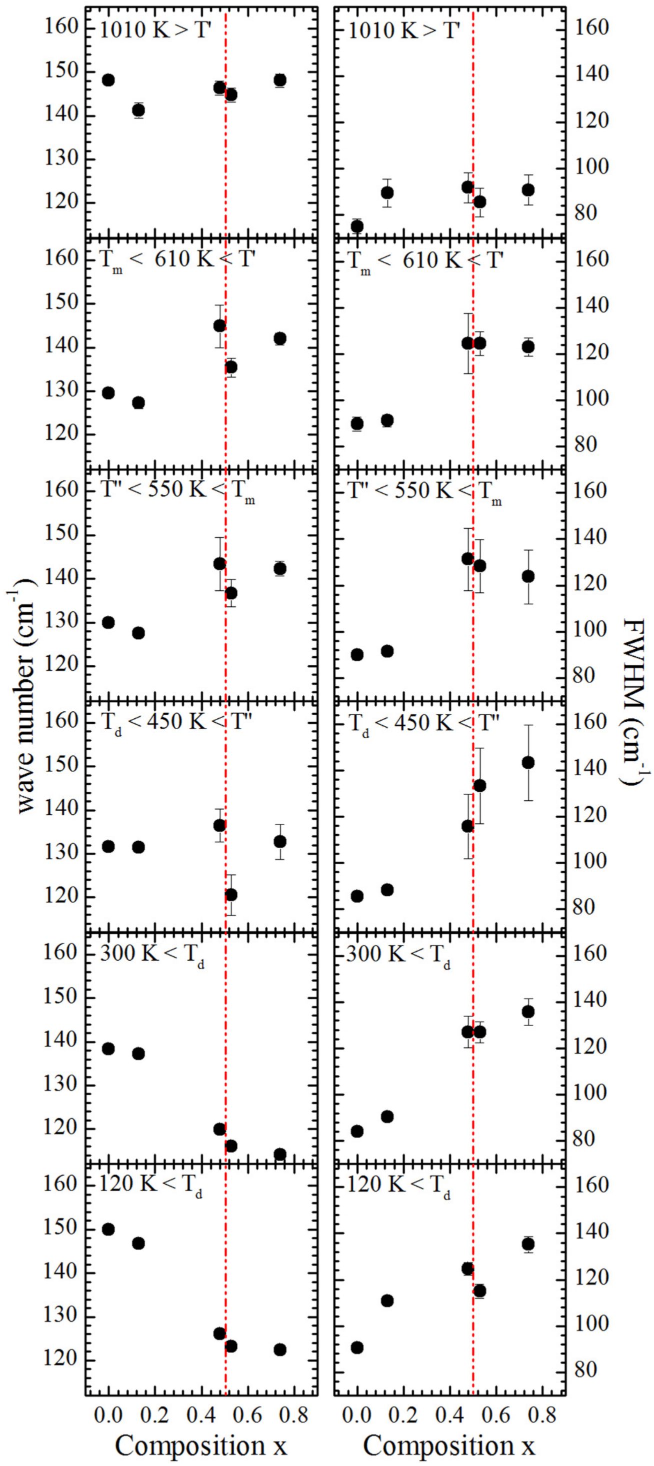

FIG. 11. Wave number ω and FWHM Γ of the Bi-TiO$_3$ mode as a function of composition x at selected fixed temperatures: 120 and 300 K $< T_d$, 450 K $\in (T_d,T'')$, 550 K $\in (T'',T_m)$, 610 K $\in (T_m,T')$, and 1010 K $> T'$.

emphasize the role of mesoscopic-scale structural correlations for the development of the complex ferroelectric state at room temperature and enhanced macroscopic properties at the MPB.

IV. CONCLUSION

The analysis of the *in situ* Raman spectra collected from NBT $-$ xBT single crystals with x=0, 0.013, 0.048, 0.053, and 0.074 from 100 to 1010 K together with room-temperature XRD data shows that MPB composition in single crystals is between 0.048 and 0.053.

The temperature evolution of phonon modes shows the following.

(i) Even at 1000 K the structure of NBT $-$ xBT is abundant with local ferroic distortions, which, however, are uncoupled, and hence the average structure appears as paraelectric cubic, although the overall ferroic distortion of the structure at 1000 K is nearly the same as that at 100 K.

(ii) For pure NBT BO$_6$ tilting is the prevailing local structural distortion at high temperatures. The temperature decrease suppresses the tilting and enhances the off-centering of BO$_6$ octahedra. These two types of ferroic distortions equalize in weight at T_m, and at T_d the BO$_6$ off centering becomes dominant, while the tilting almost disappears.

(iii) Ba doping suppresses the BO$_6$ tilting already above T_m and leads to two successive transformations associated with the A-cation off-center displacements: at T' and T'', which precede the critical temperatures T_m and T_d, respectively. It is suggested that at $T' > T_m$ AFE coupling between A-site Bi^{3+} dominates over the FE coupling, thus driving the system on further cooling to a macroscopically AFE state, whereas at $T'' \in (T_d,T_m)$ the FE coupling between A-site Bi^{3+} become dominant and drives the system to a long-range FE state developed at T_d.

(iv) The off-centered B-site Ti^{4+} cations couple at T' and the developed mesoscopic-scale FE order within the B-cation subsystem competes with the mesoscopic-scale AFE order in the A-cation subsystem for Ba-doped NBT or with the antiferrodistortive tilt order for pure NBT.

(v) At $x < x_{\mathrm{MPB}}$ the off-centered displacements of A-sites remain incoherent with those of B-site cations in the entire temperature range; only when the Ba content reaches x_{MPB} do the two subsystems become concurrent, which explains the enhancement of properties at the MPB.

(vi) The overall ferroic distortion has a minimum at the MPB because at x_{MPB} the FE coupling between B-site Ti^{4+} cations is reduced to a greater extent than the enhancement of ferroelectric A-site Bi^{3+} cations; this unique feature may be the atomistic explanation why the properties of NBT $-$ xBT at the MPB are not as good as those of Pb-based ferroelectric solid solutions [1].

ACKNOWLEDGMENTS

G.F. is indebted to the Basque Government (Grant No. POS_2015_1_0025) for a postdoctoral fellowship. The research was partially supported by the Deutsche Forschungsgemeinschaft (Grant No. MI 1127/8-1). The authors would like to thank Manfred Mühlberg and Michael Woll, University of Cologne, for synthesizing single crystals, and Stefanie Heidrich, University of Hamburg, for help with EMPA.

[1] T. Takenaka, K. Maruyama, and K. Sakata, Jpn. J. Appl. Phys. **30**, 2236 (1991).

[2] L. Luo, W. Ge, J. Li, D. Viehland, C. Farley, R. Bodnar, Q. Zhang, and H. Luo, J. Appl. Phys. **109**, 113507 (2011).

[3] W. Ge, H. Cao, C. DeVreugd, J. Li, and D. Viehland, J. Am. Ceram. Soc. **94**, 3084 (2011).

[4] I. P. Pronin, P. P. Syrnikov, V. A. Isupov, V. M. Egorov, N. V. Zaitseva, and A. F. Ioffe, Ferroelectrics **25**, 395 (1980).

[5] V. Dorcet, G. Trolliard, and P. Boullay, Chem. Mater. **20**, 5061 (2008).

[6] V. Dorcet and G. Trolliard, Chem. Mater. **20**, 5074 (2008).

[7] G. O. Jones and P. A. Thomas, Acta Crystallogr. Sect. B **58**, 168 (2002).

[8] J. Suchanicz, U. Lewczuk, and K. Koniecznya, Ferroelectrics **497**, 85 (2016).

[9] P. G. Groszewicz, M. Gröting, H. Breitzke, W. Jo, K. Albe, G. Buntkowsky, and J. Rödel, Sci. Rep. **6**, 31739 (2016).

[10] F. Cordero, Materials **8**, 8195 (2015).

[11] Q. Zhang, X. Zhao, R. Sun, and H. Luo, Phys. Status Solidi A **208**, 1012 (2011).

[12] U. Lewczuk-Jodlowiec, J. Suchanicz, D. Sitko, and K. Konieczny, Phase Transitions **90**, 818 (2017).

[13] F. Cordero, F. Craciun, F. Trequattrini, E. Mercadelli, and C. Galassi, Phys. Rev. B **81**, 144124 (2010).

[14] S.-J. L. Kang, J.-H. Park, S.-Y. Ko, and H.-Y. Lee, J. Am. Ceram. Soc. **98**, 347 (2015).

[15] S. Gorfman and P. A. Thomas, J. Appl. Crystallogr. **43**, 1409 (2010).

[16] E. Aksel, J. S. Forester, J. L. Jones, P. A. Thomas, K. Page, and M. R. Suchome, Appl. Phys. Lett. **98**, 152901 (2011).

[17] E. Aksel, J. S. Forrester, J. C. Nino, K. Page, D. P. Shoemaker, and J. L. Jones, Phys. Rev. B **87**, 104113 (2013).

[18] B. N. Rao and R. Ranjan, Phys. Rev. B **86**, 134103 (2012).

[19] S. Gorfman, A. M. Glazer, Y. Noguchi, M. Miyayama, H. Luo, and P. A. Thomas, J. Appl. Crystallogr. **45**, 444 (2012).

[20] C. Ma, H. Guo, and X. Tan, Adv. Funct. Mater. **23**, 5261 (2013).

[21] R. Ranjan and A. Dviwedi, Solid State Commun. **135**, 394 (2005).

[22] J. Y. Yi and J.-K. Lee, J. Phys. D **44**, 415303 (2011).

[23] D. Maurya, A. Pramanick, M. Feygenson, J. C. Neuefeind, R. J. Bodnar, and S. Priya, J. Mat. Chem. C **2**, 8423 (2014).

[24] S. R. Kanuru, K. Baskar, R. Dhanasekaran, and B. Kumar, J. Cryst. Growth **441**, 64 (2016).

[25] J. Suchanicz, T. V. Kruzina, V. G. Pozdeev, and S. Popov, Phase Transitions **89**, 310 (2016).

[26] C. Ma, X. Tan, E. Dul'kin, and M. Roth, J. Appl. Phys. **108**, 104105 (2010).

[27] A. A. Bokov and Z.-G. Ye, J. Mater. Sci. **41**, 31 (2006).

[28] X. Zhao, W. Qu, X. Tan, A. A. Bokov, and Z.-G. Ye, Phys. Rev. B **75**, 104106 (2007).

[29] N. Waeselmann, B. Mihailova, B. J. Maier, C. Paulmann, M. Gospodinov, V. Marinova, and U. Bismayer, Phys. Rev. B **83**, 214104 (2011).

[30] B. Mihailova, B. J. Maier, T. Steilmann, E. Dul'kin, and M. Roth, IEEE T. Ultrason. Ferroelectric Freq. Control **62**, 7 (2015).

[31] E. Husson, Key Eng. Mater. **155-156**, 1 (1998).

[32] T. Shigenari, *Raman Spectra of Soft Modes in Ferroelectric Crystals, Ferroelectric Materials—Synthesis and Characterization* (INTECH, Rijeka, 2015), Chap. 1, pp. 1–32.

[33] M. E. Marssi and H. Dammak, Solid State Commun. **142**, 487 (2007).

[34] B. Wilfong, M. Ahart, S. A. Gramsh, C. Stock, X. Li, H. Luo, and R. J. Hemley, J. Raman Spectrosc. **47**, 227 (2016).

[35] T. Steilmann, B. J. Maier, M. Gospodinov, U. Bismayer, and B. Mihailova, J. Phys.: Condens. Matter **26**, 175401 (2014).

[36] D. Rout, K.-S. Moon, J. Park, and S.-J. L. Kang, Current Appl. Phys. **13**, 1988 (2013).

[37] K. Datta, A. Richter, M. Göbbels, R. B. Neder, and B. Mihailova, Phys. Rev. B **90**, 064112 (2014).

[38] R. Loudon, Adv. Phys. **13**, 423 (1964).

[39] M. Woll, M. Burianek, D. Klimm, S. Gorfman, and M. Mühlberg, J. Cryst. Growth **401**, 351 (2014).

[40] A. M. M. Schreurs, X. Xian, and L. M. J. Kroon-Batenburg, J. Appl. Crystallogr. **43**, 70 (2010).

[41] E. Dul'kin, E. Majoev, and M. Roth, Appl. Phys. Lett. **92**, 012904 (2008).

[42] W. Jo, J. E. Daniels, J. L. Jones, X. Tan, P. A. Thomas, D. Damjanovic, and J. Rödel, J. Appl. Phys. **109**, 014110 (2011).

[43] G. de la Flor, Ph.D. thesis, University of the Basque Country UPV/EHU, 2013.

[44] A.-M. Welsch, B. J. Maier, B. M. abd R. J. Angel, J. Zhao, C. Paulmann, J. M. Engel, M. Gospodinov, V. Marinova, and U. Bismayer, Z. Kristall. **226**, 126 (2011).

[45] K. Datta, A. Richter, M. Göbbels, R. B. Neder, and B. Mihailova, Phys. Rev. B **92**, 024107 (2015).

[46] B. Mihailova, U. Bismayer, B. Güttler, M. Gospodinov, and L. Konstantinov, J. Phys.: Condens. Matter **14**, 1091 (2002).

[47] U. Bismayer, Phase Transitions **27**, 211 (1990).

[48] A.-M. Welsch, B. J. Maier, J. M. Engel, B. Mihailova, R. J. Angel, C. Paulmann, M. Gospodinov, A. Friedrich, R. Stosch, B. Güttler, D. Petrova, and U. U. Bismayer, Phys. Rev. B **80**, 104118 (2009).

[49] B. Mihailova, B. Maier, C. Paulmann, T. Malcherek, J. Ihringer, M. Gospodinov, R. Stosch, B. Güttler, and U. Bismayer, Phys. Rev. B **77**, 174106 (2008).

[50] B. Maier, B. Mihailova, C. Paulmann, J. Ihringer, M. Gospodinov, R. Stosch, B. Güttler, and U. Bismayer, Phys. Rev. B **79**, 224108 (2009).

[51] B. J. Maier, R. J. Angel, W. G. Marshall, B. Mihailova, C. Paulmann, J. M. Engel, M. Gospodinov, A.-M. Welsch, D. Petrova, and U. Bismayer, Acta Cryst. B **66**, 280 (2010).

[52] B. Mihailova, N. Waeselmann, B. Maier, B. A.-M, Welsch, R. Angel, and U. Bismayer, High Press. Res. **33**, 595 (2013).

[53] J. Petzelt, D. Nuzhnyy, V. Bovtun, M. Paściak, S. Kamba, R. Duttner, S. Svirskas, J. Banys, and J. Rödel, Phase Transitions **87**, 953 (2014).

[54] I. G. Siny, E. Husson, J. M. Beny, S. G. Lushnikov, E. A. Rogacheva, and P. P. Syrnikov, Physica B **293**, 382 (2001).

[55] E. Dul'kin, J. Tiagunova, E. Mojaev, and M. Roth, Functional Mater. Lett. **10**, 1750048 (2017).

[56] J. Toulouse, F. Jiang, O. Svitelskiy, W. Chen, and Z.-G. Ye, Phys. Rev. B **72**, 184106 (2005).